GPS Solutions (2026) 30:7
https://doi.org/10.1007/s10291-025-01976-9

RESEARCH

Ionospheric nonlinear interpolation model for Mid- and Low-latitude network RTK during solar maxima

Tong Liu[1] · Wu Chen[1] · Xiaolong Mi[1] · Xingyu Chen[1,2] · Yang Yang[1] · Junsheng Ding[1] · Tianxia Liu[1] · Yuyan Wang[1] · Duojie Weng[3]

Received: 25 June 2025 / Accepted: 3 October 2025

Abstract

As the Sun approaches the peak of its 25th activity cycle, intensified ionospheric spatial gradients near the equatorial ionization anomaly (EIA) crest pose critical challenges to GNSS positioning accuracy, particularly in low-latitude regions. Traditional network RTK systems, which rely on linear interpolation models (LIMs) to approximate ionospheric correlations between reference stations, inadequately resolve nonlinear spatial gradients along ionospheric pierce point (IPP) trajectories, a key source of residual errors in double-differenced ionospheric (DDI) delays. To address this limitation, we introduce a Nonlinear Interpolation Model (NIM) that explicitly incorporates satellite-specific gradients along IPP trajectories. By dynamically detrending spatially nonlinear ionospheric terms, NIM improves ionospheric delay interpolation accuracy. Evaluations across mid-latitude and low-latitude networks show NIM reduces DDI interpolation errors by 30–40% compared to LIMs. Statistical analyses under diverse ionospheric conditions highlight NIM's enhanced error distribution characteristics, particularly during sunset and post-sunset transitions when gradients peak. Notably, during the extreme May 2024 geomagnetic storm, NIM achieved below 2 cm RMS positioning accuracy in Hong Kong, a region historically prone to large ionospheric gradients. These improvements translate to measurable gains: a 10% higher ambiguity resolution success rate, 30% faster convergence times, and horizontal/vertical positioning precision of 1.1/3.8 cm. By integrating IPP trajectory gradients into spatial modeling, NIM provides a scalable framework for robust RTK operations in gradient-prone regions. This advancement supports reliable centimeter-level positioning during solar maxima.

Keywords GNSS · Network RTK · Ionospheric delay · Low latitude · Nonlinear interpolation · Solar maxima

✉ Xiaolong Mi
xiaolong.mi@polyu.edu.hk

Tong Liu
tong2.liu@polyu.edu.hk

Wu Chen
wu.chen@polyu.edu.hk

Xingyu Chen
xingyu-max.chen@polyu.edu.hk

Yang Yang
yyoung.yang@polyu.edu.hk

Junsheng Ding
junsheng.ding@polyu.edu.hk

Tianxia Liu
tianxia.liu@connect.polyu.hk

Yuyan Wang
yuyan16.wang@connect.polyu.hk

Duojie Weng
djweng@szu.edu.cn

[1] Department of Land Surveying and Geo-Informatics, The Hong Kong Polytechnic University, Hong Kong, China

[2] The Innovation Academy for Precision Measurement Science and Technology of the Chinese Academy of Sciences, Wu Han, China

[3] Ministry of Natural Resources (MNR) Key Laboratory for Geo-Environmental Monitoring of Great Bay Area & Guangdong Key Laboratory of Urban Informatics, Shenzhen University, Shenzhen, China

Published online: 18 October 2025

Introduction

Solar radiation induces plasma that diffuses from high-density equatorial regions toward mid- and low-latitude areas, forming the equatorial ionization anomaly (EIA) with peak total electron content (TEC) near ± 15° magnetic latitude (Mitra 1946; Martyn 1955). This process generates significant anisotropic ionospheric spatial gradients, which compromise the accuracy of ionospheric corrections broadcast by the Global Navigation Satellite System (GNSS) ground infrastructure. These inaccuracies are particularly pronounced in real-time kinematic (RTK) positioning systems, where ionospheric delay errors can exceed one meter for baselines spanning several kilometers (Weng et al. 2015). During periods of heightened solar activity, such errors are amplified, frequently leading to degraded or failed RTK services. Consequently, high-precision applications reliant on RTK, including drone swarm operations, deformation monitoring, surveying, autonomous driving, and mobile positioning, are facing severe operational limitations at low latitudes.

The growing availability of ground-based observations across multiple baselines could contribute to modeling the distance-dependent ionospheric delays in modern network RTK systems. For baselines within a few tens of kilometers in length, the accurate double-differenced ionospheric delays (DDI) between reference stations could be achieved once double-differenced integer ambiguities are resolved (St-Pierre 1999; W. Chen et al. 2001b). However, accurately interpolating these DDIs to the user's location remains a challenge.

Simple interpolation methods, such as inverse distance weighting (IDW), rely solely on distance between as a detrending factor and fail to account for ionospheric spatial gradients. The linear interpolation model (LIM), which incorporates station coordinates into spatial modeling, was introduced to address this limitation (Wanninger 1995b, a). Subsequent extensions of LIM, including low-order polynomial and surface models, have shown marginal improvements (Wübbena et al. 1996; Fotopoulos 2000), while advanced techniques like least squares collocation and kriging similarly struggle to surpass LIM's performance (Dai et al. 2003; Al-Shaery et al. 2011).

Despite its widespread adoption and centimeter-level accuracy for short baselines in middle latitude (Vollath et al. 2000; P. Wang et al. 2023), LIM exhibits significant limitations in networks with long baselines or regions of pronounced ionospheric gradients, such as low-latitude areas (Tang et al. 2016; Cui et al. 2018). In these scenarios, inaccuracies in ionospheric delay interpolation often degrade ambiguity resolution (Saraçoğlu 2024; J. Zhang et al. 2024a, b), leaving the challenge of reliable ionospheric corrections in high-gradient regions unresolved.

Recent advances in ionospheric interpolation, though not explicitly designed for network RTK, offer promising insights. For instance, a single-satellite methods have improved slant TEC modeling accuracy (W. Li et al. 2022a, b), while piecewise linear transformations (Cheng et al. 2024), radial basis functions (RBFs) (L. Yang et al. 2024a, b), recurrent feature reasoning (Sun et al. 2025a), and advanced kriging techniques for regional (W. Zhang et al. 2024a, b), wide-area (A. Liu et al. 2024a, b; Ren et al. 2024) and global (H. Lyu et al. 2024) mapping. Parallel developments in Precise Point Positioning (PPP) and PPP-RTK demonstrate that external ionospheric constraints can mitigate positioning errors during disturbances (Zhang et al. 2022). Further refinements, such as cross-validated uncertainty models (P. Li et al. 2022a, b), enhanced grid-based adjustments (Li et al. 2023; S. Lyu et al. 2023), have strengthened PPP-RTK robustness under dynamic ionospheric conditions. These works, particularly those leveraging ionospheric pierce point (IPP) trajectories and satellite-specific slant TEC, provide valuable insights for advancing network RTK systems.

Crucially, DDI exhibit dual dependencies, that is, not only on receiver station coordinates but also on the dynamic geometry of IPPs (Tang et al. 2016; Cui et al. 2018). The EIA affected regions present particularly pronounced ionospheric gradients along IPP trajectories, driven by the highly nonlinear spatiotemporal distribution of TEC (Nigussie et al. 2022; He et al. 2024). Notably, the single-difference between satellites inherently transfers these gradients into DDI estimates, creating systematic biases that conventional LIM cannot fully mitigate (Hong et al. 2022; Slamet et al. 2022). While LIM effectively addresses station-related linear gradients through single-epoch spatial modeling, it neglects the nonlinear spatial gradients associated between IPPs (Cui et al. 2018; J. Chen et al. 2024). These residual nonlinear gradients persist after double difference and LIM processing, manifesting as independent errors of station coordinates that LIM cannot resolve.

To overcome this issue, we propose a Nonlinear Interpolation Model (NIM) that explicitly accounts for gradients along IPP trajectory. Building upon gradient along the IPP movement (GAIM), NIM introduces a novel detrending mechanism by treating IPP positions as independent spatial variables (Shi et al. 2022; J. Chen et al. 2024). This dual-function methodology enables: (1) precise separation of nonlinear ionospheric gradients from station-dependent errors, and (2) enhanced ambiguity resolution and positioning accuracy through improved spatial correlation modeling. The remainder of this paper is organized as follows: Sect. "Problem" provides a theoretical analysis of the nonlinear gradient problem, followed by the mathematical

formulation of our proposed framework in Sect. "Method". The following Sects. "Data and processing settings"–"Interpolation accuracy" conducts systematic experimental validation through multi-scenario GNSS datasets, performs benchmark comparisons with quantitative error analysis. Finally, we discuss and conclude the advantages and limitations of NIM.

Problem

To clarify the problem, this section describes the nonlinear terms in the residual ionosphere delay from theoretical and observation, respectively.

The unmodeled ionospheric gradients of current RTK

GNSS signals are transmitted from satellites and traverse through the IPPs before being received by ground stations located at various positions, denoted as (x, y). For each unique pairing of a station and a satellite, the ionospheric delay, denoted as I, can be mathematically expressed as a function of the IPP's position, which can be written as $I=f(x, y)$. A sketch map of spatial differences of the ionospheric TEC map can be seen in Fig. 1.

For a certain epoch, the double differenced ionospheric delay can be mathematically expressed in Eq. (1). The single-difference between satellites quantifies the ionospheric differences between the pierce points (i and j) of the same ground station, whereas the single-difference between stations accounts for the ionospheric differences between different ground stations (m and n) of the same satellite. That is, the resulting double-difference both captures the ionospheric differences among stations and satellites.

$$\begin{aligned}\Delta\nabla I &= \Delta\nabla f(x_{m-n}^{i-j}, y_{m-n}^{i-j}) \\ &= \nabla f(x_m^{i-j}, y_m^{i-j}) - \nabla f(x_n^{i-j}, y_n^{i-j}) \\ &= [f(x_m^i, y_m^i) - f(x_m^j, y_m^j)] - [f(x_n^i, y_n^i) - f(x_n^j, y_n^j)]\end{aligned} \tag{1}$$

where, $\Delta\nabla$ denotes the double-differencing operation, i.e., Δ represents the single difference between stations and ∇ represents the single difference between satellites; x and y represent longitude and latitude respectively; superscripts i, j denote the satellites at ionospheric pierce points and subscripts m, n denotes the station numbers.

The ionospheric difference between stations already modeled by LIM, is highlighted in blue and the unmodeled ionospheric difference between satellites, is highlighted in red are illustrated in Fig. 2. Subsequent Fig. 3 presents the double difference ionospheric delays between HKST and HKSC stations over a full day, alongside the S4 index calculated from signal-to-noise ratio (SNR) measurements (Luo et al. 2020a) during the same period. When ionospheric scintillation occurs, poor-quality carrier-phase observations between reference stations prevent the calculation of high-precision double differenced ionospheric delays, rendering interpolation efforts ineffective. Conversely, in the absence of scintillation, accurate dual-difference ionospheric delays can be reliably computed between reference stations, enabling precise interpolation at the user end.

Figure 3a demonstrates pronounced double-differenced ionospheric gradient characteristics (W. Chen et al. 2001a), particularly evident during the sunset transition period and post-sunset hours. This ionospheric error in double difference frequently causing the estimation accuracy to reach or

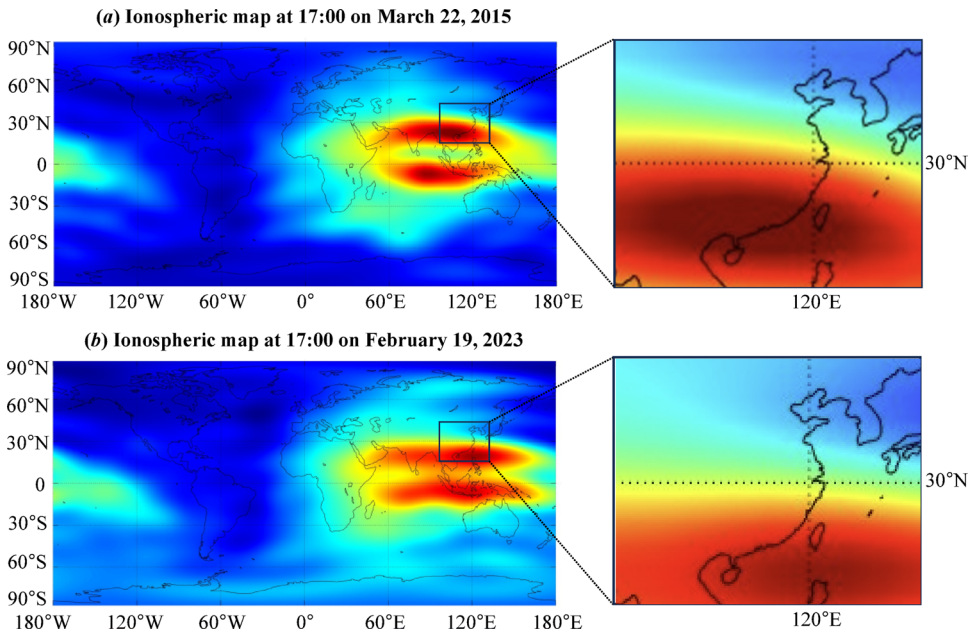

Fig. 1 Ionospheric maps from the Center for Orbit Determination in Europe (CODE): **a** Map at 17:00 UTC, March 22, 2015; **b** Map at 17:00 UTC, February 19, 2023

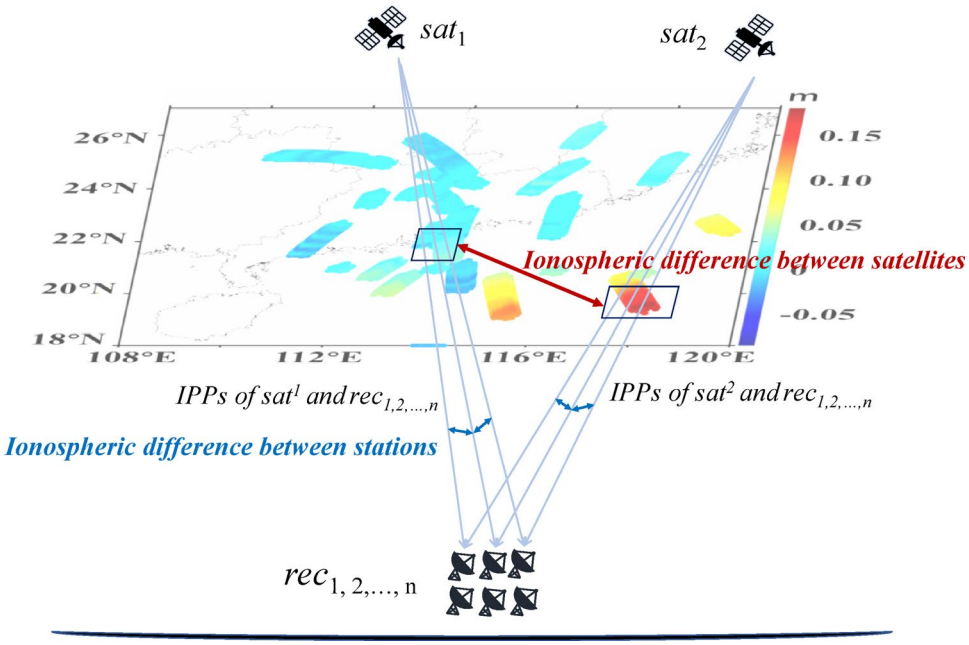

Fig. 2 A schematic diagram illustrating ionospheric differences between satellites and between stations. During the double-difference process, in addition to the ionospheric discrepancies between stations, as labeled in blue text, the ionospheric discrepancies between satellites are also incorporated, as marked in red text

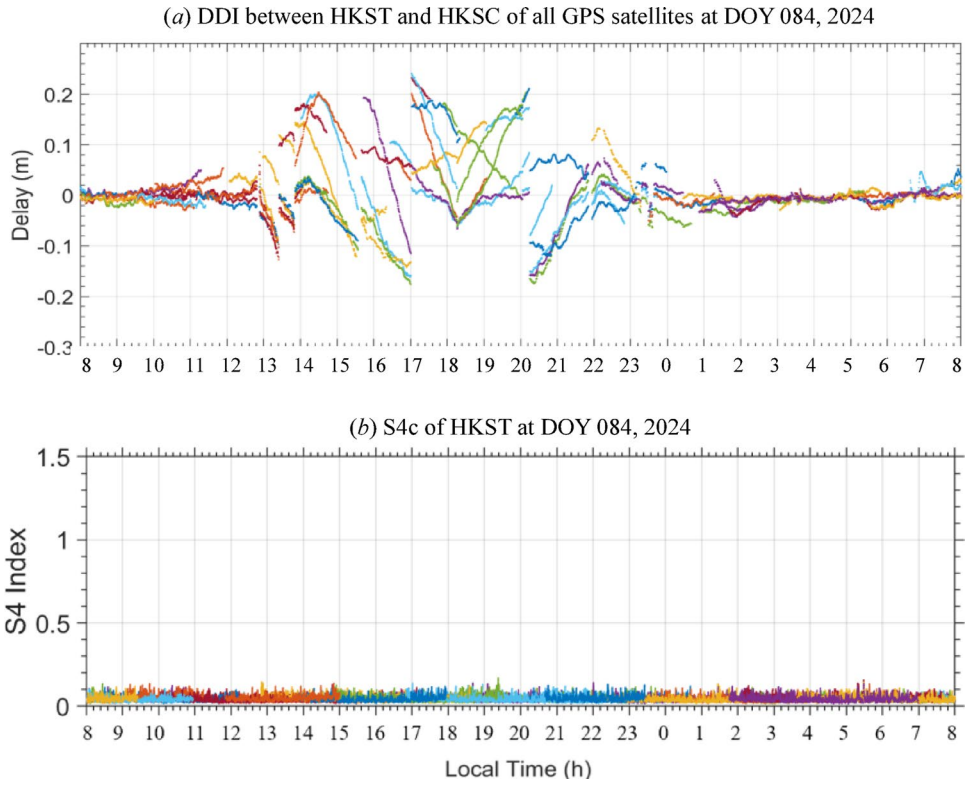

Fig. 3 Double differenced ionospheric delay and S4 index observed on DOY 84, 2024. Horizontal axis denotes local time, vertical axis **a** shows delay at L1 frequency and **b** shows the amplitude scintillation, with color-coding distinguishing satellite-specific variations

exceed 1/4 of the L1 wavelength. In such cases, ambiguity resolution becomes significantly more challenging (Zhu 2019; Zhu et al. 2023), posing a critical obstacle for network RTK applications. To clearly distinguish from existing station coordinate-based LIM models, we define the delay component unmodeled by LIM, which is independent of station coordinates, as the ionospheric nonlinear term.

The ionospheric gradient along IPPs

Further, we need to know the source of the delay related to DDI. From a satellite view, at a specific epoch, the tangential vector of the IPP trajectory effectively captures its ionospheric gradient. That is, the residual non-linear ionospheric gradient along the IPPs can be achieved based on the time-differenced geometry-free combinations of carrier

phase observations and the IPP distance, i.e., gradient along the IPP movement (GAIM) (Weng et al. 2015) can be easily calculated as:

$$\mathrm{GAIM} = \frac{\phi_4(t) - \phi_4(t - t_0)}{(\gamma - 1) \cdot d_{\mathrm{IPP}}} \tag{2}$$

where, ϕ is the geometry-free combination of dual-frequency carrier phase observations (ϕ_1 and ϕ_2). d_{IPP} is the distance of IPPs of each satellite between epoch t and epoch t-1. γ is the conversion factor, i.e., f_1^2/f_2^2.

Figure 4 provide an intuitive illustration of this issue. For short baselines in regions far from the EIA, ionospheric gradients are typically linear, stable, and exhibit minimal spatiotemporal variation. However, in low-latitude areas such as Hong Kong or over long baselines in mid-latitudes, significant gradients are observed. Figure 4a illustrates how ionospheric gradients, induced by IPP, contribute to double-differenced ionospheric delays: As Sat^1 moves to the position of $Sat^{1'}$, it observes spatial ionospheric variations distinct from those of Sat^2. Figure 4b shows the ionospheric gradients along IPPs of all GPS satellites on March 24, 2024, and Fig. 4c shows its spatial variations.

(*a*) Schematic introduction of nonlinear spatial gradients by satellite motion

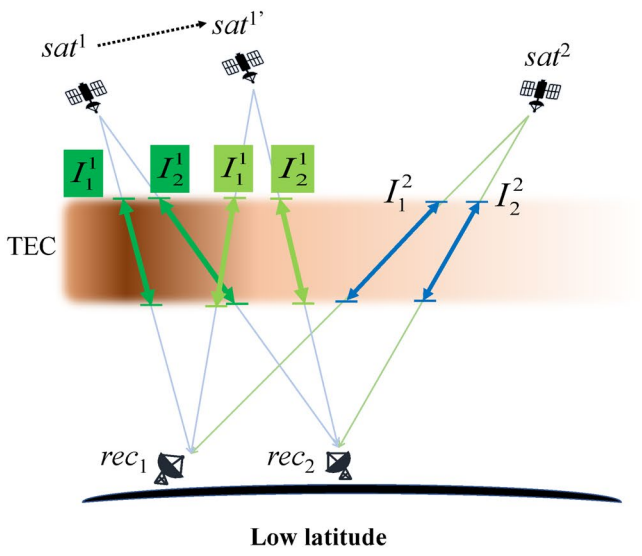

(*b*) Ionospheric gradient presented as time series

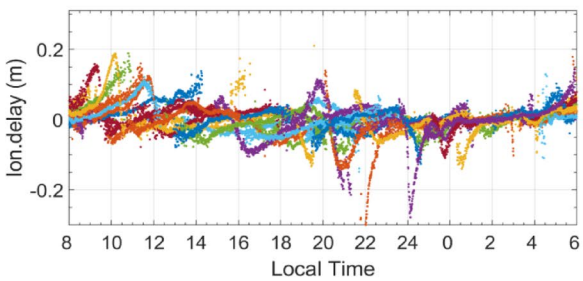

(*c*) Ionospheric gradient presented as spatial sequence

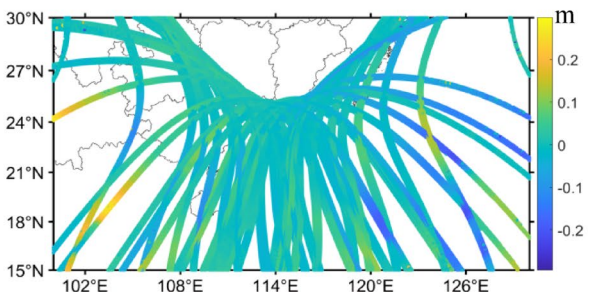

Fig. 4 Overview of ionospheric nonlinear gradient variations: **a** Schematic of double-differencing calculations; **b** Ionospheric gradients with time-differenced geometry-free combination in Hong Kong, 2024; **c** Ionospheric gradients vs. IPPs, with color indicating gradient magnitude (units: meters in GF combination)

Method

To address the nonlinear ionospheric errors in network RTK, we introduce the NIM. This section will delve into the development of the nonlinear composite functional model, present the solution to NIM, and provide the data processing workflow.

The composite function model

The composite function employs a dual-layer function to address spatial dependencies at distinct scales. The framework is constructed as follows:

(1) The outer function- correlation between the station coordinates and DDI.

Equation (1) represents the double-difference ionospheric delay between the satellites of user and the master stations. We now extend it to include all ground reference stations of a network. After the double-differencing process, a new function, $\Delta\nabla f$, depends on the sequence of IPPs from single-difference between satellites, represented by $\boldsymbol{v}^{\mathrm{sat}}$, i.e., ($\boldsymbol{v}^{1,2,\ldots,i}$ and $\boldsymbol{v}^{j}$) or (x^{1-j}, x^{2-j}, …, x^{i-j}; y^{1-j}, y^{2-j}, …, y^{i-j})' and from single-difference between stations, represented by $\boldsymbol{v}_{\mathrm{rec}}$, i.e., ($\boldsymbol{v}_{1,2,\ldots,m}$ and $\boldsymbol{v}_n$) or ($x_{1\text{-}n}$, $x_{2\text{-}n}$, …, $x_{m\text{-}n}$; $y_{1\text{-}n}$, $y_{2\text{-}n}$, …, $y_{m\text{-}n}$)', is formed. Initially, we qualitatively express the double differenced delay $\boldsymbol{I}$ across all stations as:

$$\Delta\nabla \mathbf{I} = \Delta\nabla f(\mathbf{v}^{sat}, \mathbf{v}_{rec}) \tag{3}$$

Then, we expanding Eq. (1), analogous to Eq. (1), to describe the double difference operation applied to the observations from different satellites and different stations. If do single difference between satellites first, then the single difference between stations, we can express the overall function model of NIM as:

$$\begin{aligned} &\Delta\nabla f\left(v_{sat}, v_{rec}\right) \\ &= \left[f(v^{1,2,\ldots,i}) - f(v^{j})\right]_{1,2,\ldots,m} \\ &-\left[f(v^{1,2,\ldots,i}) - f(v^{j})\right]_{n} \\ &= g_{rec}\left[h^{sat}\left(v^{sat}, v_{rec}\right)\right] \end{aligned} \tag{4}$$

where, the function g_{rec} is function related only on the station coordinates $\boldsymbol{v}_{\text{rec}}$; the function h^{sat} is a function related only on the satellite coordinates $\boldsymbol{v}^{\text{sat}}$.

In traditional LIM, there is an implicit assumption that $\Delta\nabla f$ is equivalent to the outer function g_{rec}, meaning the double-differenced ionospheric delay is only a linear or planar function of the station coordinates. Based on this assumption, for satellites i and reference satellite j, across all stations (1, 2, …, m) can be easily derived. i.e.:

$$\Delta\nabla f\left(v^{sat}, v_{rec}\right) = g_{rec}\left(v_{rec}\right) \tag{5}$$

Then, the linear ionospheric delay related to station coordinates can be calculated (Wanninger 1995a, b).

(2) The inner function- correlation between the IPPs and DDI.

As discussed in the second section, ionospheric gradients along IPPs between satellites could cause accuracy loss in the final DDI estimation by LIM. For short baselines in mid-latitude regions, where the single differences of ionospheric gradient between satellite and between station are largely consistent, that is, using the sequence of station coordinates as the independent variable matrix is sufficient for modeling, making the LIM adequate. However, in low-latitude regions, as shown in Fig. 4a, the gradients between satellite (sat^1 and sat^2) are independent from the receiver coordinates. Therefore, both g_{rec} and h^{sat} should be considered to address this issue effectively. Therefore, Eq. (3) should be rewritten as:

$$\begin{aligned} &\Delta\nabla f\left(v^{sat}, v_{rec}\right) \\ &= g_{rec}\left(v_{rec}\right) \cdot h^{sat}\left(v^{sat}\right) \\ &= g_{rec}\left(\begin{bmatrix} x_{1-n} & y_{1-n} \\ x_{2-n} & y_{2-n} \\ \vdots & \vdots \\ x_{m-1-n} & y_{m-1-n} \end{bmatrix}\right) \cdot h^{sat}\left(\begin{bmatrix} x^{1-j} & y^{1-j} \\ x^{2-j} & y^{2-j} \\ \vdots & \vdots \\ x^{i-j} & y^{i-j} \end{bmatrix}\right) \end{aligned} \tag{6}$$

In contrast to the traditional LIM method that relies on station coordinates, the new composite function innovates by adopting differences between satellites as additional independent variable. As a consequence, the ionospheric gradients between satellites are detrended utilizing the inter-satellite distances, i.e., the IPP differences. This shift necessitates the development of a novel functional framework that builds upon the LIM methodology by incorporating an additional layer of computation. This strategic layering facilitates the breakdown of the composite function into two distinct functions, enabling a step-by-step interpolation solution.

The solution of NIM function

The next challenge is solving Eq. (4). This section examines the relationship between LIM-modelable delays and non-linear delays, and outlines the solution for the model after integrating GAIM.

(1) Separate the linear ionospheric delay and nonlinear ionospheric delay.

To clearly separating the interdependencies between station coordinates, IPP distance and DDI. We further clarify this with additional formulaic derivations:

$$\begin{aligned} &\frac{\partial^2}{\partial(v^{sat}, v_{rec})}\Delta\nabla I = \frac{\partial^2}{\partial x_{m-n}\partial y_{m-n}}\left(\frac{\partial^2}{\partial x_{i-j}\partial y_{i-j}}\Delta\nabla I\right) \\ &= \frac{\partial^2}{\partial x_{m-n}\partial y_{m-n}}\left(\frac{\partial^2}{\partial x^{i-j}\partial y^{i-j}}\left(\Delta\nabla I_{rec} + \Delta\nabla I_{sat}\right)\right) \\ &= \frac{\partial^2}{\partial x_{m-n}\partial y_{m-n}}\left(\frac{\partial^2}{\partial x^{i-j}\partial y^{i-j}}\left(\Delta\nabla I_{linear} + \Delta\nabla I_{non-linear}\right)\right) \\ &= \frac{\partial^2}{\partial x_{m-n}\partial y_{m-n}}\left(\Delta\nabla I_{linear} + \frac{\partial^2}{\partial x^{i-j}\partial y^{i-j}}\Delta\nabla I_{non-linear}\right) \end{aligned} \tag{7}$$

where, $\boldsymbol{I}_{\text{rec}}$ and $\boldsymbol{I}^{\text{sat}}$ represent the ionospheric delays vector associated with the station coordinates vector ($x_{m\text{-}n}$, $y_{m\text{-}n}$) and the IPP distances vector (x^{i-j}, y^{i-j}) respectively. $\boldsymbol{I}_{\text{linear}}$ and $\boldsymbol{I}^{\text{non-linear}}$ represent the linear and non-linear ionospheric delays vector.

Equation (5) explains that during the process of double-difference, if first performing single differences between satellites followed by single difference between stations, it introduces a correlation between $\boldsymbol{I}^{\text{sat}}$ and the station coordinates. Consequently, $\boldsymbol{I}^{\text{sat}}$ is correlated with both ($x_{m\text{-}n}$, $y_{m\text{-}n}$) and (x^{i-j}, y^{i-j}). This makes it difficult to solve this function. To simplify this dual dependency and build a connection to LIM, the terms both of $\boldsymbol{I}_{\text{rec}}$ and $\boldsymbol{I}^{\text{sat}}$ related with ($x_{m\text{-}n}$, $y_{m\text{-}n}$) are reshaped as $\boldsymbol{I}_{\text{linear}}$, the terms of $\boldsymbol{I}^{\text{sat}}$ that is related with (x^{i-j}, y^{i-j}) are reshaped as $\boldsymbol{I}_{\text{non-linear}}$.

The linear terms $\boldsymbol{I}_{\text{linear}}$ can be divided into two categories: one category consists of spatial terms that can be modeled through inter-station difference and can be eliminated in a

LIM at single-epoch; the other category comprises the non-linear residual after applying LIM.

(2) Solution of nonlinear terms.

We know that what LIM remains to model is $\boldsymbol{I}_{\text{non-linear}}$, i.e., the residual spatial terms between satellites, which requires to calculate the coefficient α and β of function h^{sat} in Eq. (4). Fortunately, as mentioned in Sect. "The ionospheric gradient along IPPs", the GAIM provides a direct sensing of major part of the non-linear residuals $\boldsymbol{I}_{\text{non-linear}}$:

$$\Delta\nabla I_{\text{non-linear}} = \Delta\nabla GAIM + \varepsilon_{\text{non-linear}} \tag{8}$$

where, $\varepsilon_{\text{non-linear}}$ means the possible remaining nonlinear terms that have not yet been modeled by NIM.

Then, the relationship between $\Delta\nabla$GAIM and $\boldsymbol{v}^{\text{sat}}$ can be described and the coefficient α and β of function h^{sat} can be calculated by least squares solution:

$$\begin{bmatrix} \Delta\nabla GAIM^{1,j} \\ \Delta\nabla GAIM^{2,j} \\ \vdots \\ \Delta\nabla GAIM^{i,j} \end{bmatrix} = \begin{bmatrix} x_{IPP}^{1,j} & y_{IPP}^{1,j} \\ x_{IPP}^{2,j} & y_{IPP}^{2,j} \\ \vdots & \vdots \\ x_{IPP}^{i,j} & y_{IPP}^{i,j} \end{bmatrix} \cdot \begin{bmatrix} \alpha \\ \beta \end{bmatrix} \tag{9}$$

where, α and β are the coefficient of the planar trend between the tangential vector of IPPs trajectory.

Then, the ionospheric delay between satellites can by calculated:

$$\Delta\nabla I^{\text{sat}} = \Delta\nabla I^{i,j} = \begin{bmatrix} x^{i-j} & y^{i-j} \end{bmatrix} \begin{bmatrix} \alpha \\ \beta \end{bmatrix} \tag{10}$$

With these steps, the remaining spatial residuals between IPPs are modeled.

(3) Solution of linear terms.

Then, the matrix form of Eq. (3), as commonly seen in previous studies of LIM (Wanninger 1995a; Cui et al. 2018), can be expressed as:

$$\begin{bmatrix} \Delta\nabla I_{1,n} \\ \Delta\nabla I_{2,n} \\ \vdots \\ \Delta\nabla I_{m-1,n} \end{bmatrix} = \begin{bmatrix} x_{1-n} & y_{1-n} \\ x_{2-n} & y_{2-n} \\ \vdots & \vdots \\ x_{m-1-n} & y_{m-1-n} \end{bmatrix} \cdot \begin{bmatrix} a \\ b \end{bmatrix} \tag{11}$$

where, a and b are the coefficient of the planar or linear trend between ground stations.

Generally, we can calculate coefficients a and b and finally estimate the LIM-based DDI for users as:

$$\Delta\nabla \boldsymbol{I}_{\text{rec}} = \Delta\nabla \boldsymbol{I}_{m,n} = \begin{bmatrix} x_{m-n} & y_{m-n} \end{bmatrix} \begin{bmatrix} a \\ b \end{bmatrix} \tag{12}$$

(4) Vector sum of the gradient components.

Finally, the composite function has been successfully solved, with the final double-difference ionospheric delay comprising a vector sum of two components: a linear delay dependent on station coordinates and a nonlinear delay associated with the IPP trajectory:

$$\begin{aligned} \Delta\nabla I &= \Delta\nabla I^{i,j} + \Delta\nabla I_{m,n} \\ &= \begin{bmatrix} x^{i-j} & y^{i-j} \end{bmatrix} \begin{bmatrix} \alpha \\ \beta \end{bmatrix} + \begin{bmatrix} x_{m-n} & y_{m-n} \end{bmatrix} \begin{bmatrix} a \\ b \end{bmatrix} \end{aligned} \tag{13}$$

The data process flow of NIM

The data processing flow of NIM is depicted in Fig. 5. The inputs for this process include observations and ephemeris files from all stations within the Hong Kong CORS network.

In the first stage, reference stations, including a master station and adjacent other reference stations, are selected based on the user's approximate location within the network. The preprocessing begins with: (1) the calculation of DDI between the master and reference stations; (2) GAIM are computed using dual-frequency carrier phase observations, followed by (3) calculation of IPPs corresponding to the calculated DDI and gradients.

In the second stage, nonlinear coefficients are derived for both the master and reference stations based on GAIM and IPP data. After that, nonlinear spatial correlation coefficients of the IPPs are used to detrend the gradients between satellite within the DDI. Then, the DDI, now excluding satellite induced gradients, is applied for detrending between stations. Finally, based on the user's approximate location, the newly modeled and estimated DDI is generated by vector addition as output.

Data and processing settings

To simulate the virtual reference station (VRS) process in network RTK, we implemented the outlined steps on the VENUS platform (Zhou et al. 2019) to generate DDIs and the virtual reference station observations. The DDI between the master and reference stations are calculated and put in NIM, Then, to estimate the DDI between the master and simulated user, the NIM performance for poisoning results are evaluated on the RTKlib demo5 software (Takasu & Yasuda 2009). The DDI between the master station and simulated user was calculated as the reference value for comparison.

It is important to note that only the DDIs with successfully fixed ambiguities of baselines between reference stations are retained for further processing. When handling

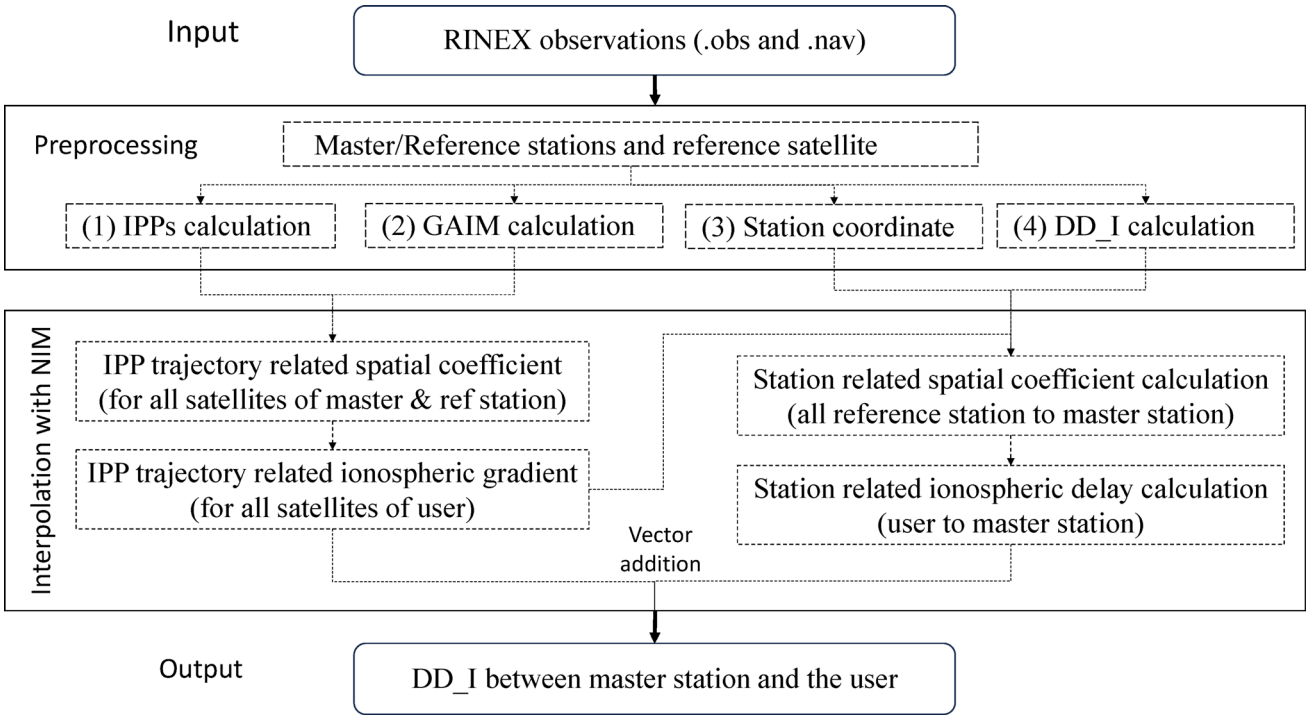

Fig. 5 Workflow of the NIM method

Table 1 Parameter and model settings for RTK positioning

Items	Strategies at system end	Strategies at user end
Observations	GPS code and phase observations	
Frequency	GPS L1 and L2	
Solution mode	Static/ Coordinate fixed	Kinematic
Ionospheric delay	Estimate	Corrected by LIM/NIM
Ionospheric pierce height	350 km	350 km
Tropospheric delay	Estimate as random-walk noise ($10^{-4} m/\sqrt{s}$); Priori value is provided by the UNB3m model; GMF is used for mapping function	
Estimator	Kalman filter	
Elevation cutoff angle	10° for excluding observations and 20° for included in ambiguity solution	
Weighting Strategy	Elevation-dependent weighting, for Code: σ_p=0.3 m; Phase: σ_ϕ=0.003 m	
Phase ambiguities	Estimated as float constants for each arc	Both instantaneous and continuous ambiguity resolution are tested
Integer ambiguity resolution	System: Wide-lane ambiguity is resolved to determine L1 and L2 (W. Chen et al. 2003) User: RTKlib demo5 with LAMBDA method with ratio threshold setting as 2.0	
Satellite involved	Fault detection and exclusion is used for data equality control (Takasu & Yasuda 2009)	
Signal-to-noise ratio mask	30 dB-Hz	

DDI computations across multiple baselines, the common reference satellite is chosen for all the baselines based on its elevation angle. Ambiguity resolution is conducted with the LAMBDA method (P. J. Teunissen 1993), with a ratio threshold of 2.0. The data sampling with 30s are used for preliminarily interpolation accuracy estimation. Then, the data sampling with 1s are tested for interpolation accuracy and positioning. The cut-off elevation angle is set to 10°.

In the positioning performance testing with continuous ambiguity resolution, the positioning calculations are initialized every minute. Convergence of the positioning results was considered achieved if the ambiguity was fixed and the horizontal and vertical errors remained below 5 cm and 10 cm, respectively, for 20 consecutive seconds (J. Zhang et al. 2024a, b). The detailed settings are shown in Table 1.

Figure 6 shows 3 datasets designed to evaluate NIM. Since reliably fixing between-receiver ambiguities proves difficult for long low-latitude baselines, making interpolation impractical, and standard linear interpolation works adequately for short mid-latitude baselines, our testing focuses specifically on long mid-latitude and short low-latitude configurations. We also prioritize evaluating NIM performance during geomagnetic storms when severe ionospheric gradients affect low latitudes. For these assessments, we established: dataset (*a*) Melbourne with mid-latitude network mostly > 20 km baselines; dataset (*b*) Hong Kong-1 with low-latitude network mostly < 20 km baselines. To enable extended storm-period analysis, we added dataset *c*

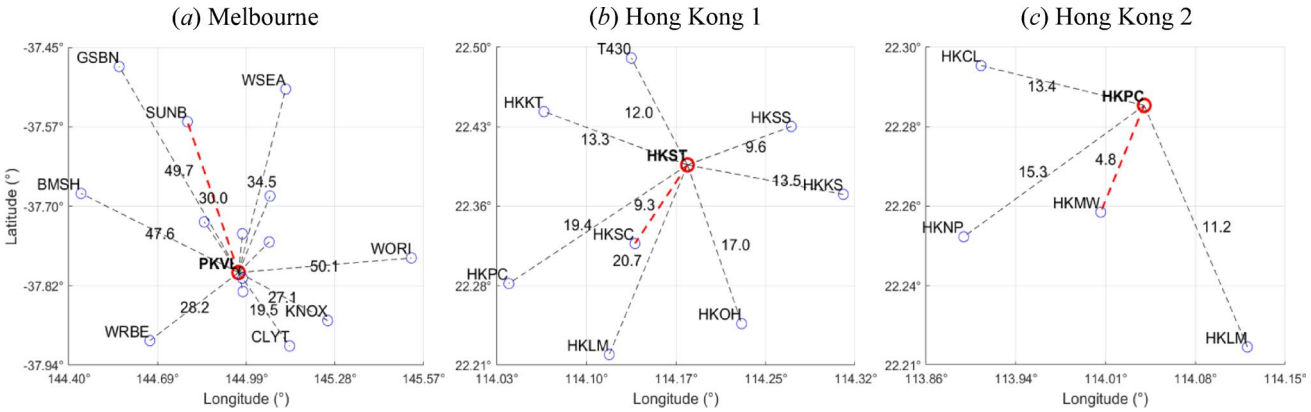

Fig. 6 The baselines and lengths of the 3 datasets

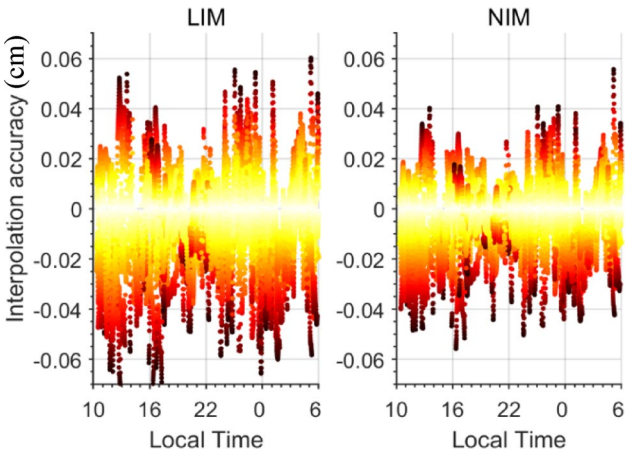

Fig. 7 Interpolation accuracy at Melbourne on May 1, 2024

Hong Kong-2, a streamlined version of HK-1 with fewer stations that reduces computation loads.

Our evaluation compares LIM and NIM with DDI results using Melbourne (long mid-latitude) and HK-1 (short low-latitude) data. HK-2 specifically tests NIM's statistical interpolation and positioning effectiveness during the May 2024 geomagnetic storm (Sun et al. 2025b) through network RTK solutions. The ambiguity resolution success rates (instantaneous/continuous), convergence times, and post-convergence positioning accuracy are tested.

Interpolation accuracy

Interpolation accuracy was evaluated at mid- and low-latitudes, and by the statistics of the extreme geomagnetic storm in May 2024.

DDI interpolation results at mid and low latitudes

Mid-latitude case (Melbourne, May 1, 2024)

The performance of the proposed NIM was first evaluated using mid-latitude data from Melbourne on May 1, 2024. With PKVL as the master station and SUNB as the user station (baselines: 10–50 km), NIM demonstrated superior precision compared to the traditional LIM. As illustrated in Fig. 7, NIM confined interpolation errors to ± 4 cm, outperforming LIM's ± 6 cm range. Notably, NIM showed marked improvements during periods of elevated ionospheric activity (13:00, 16:00, and pre-00:00), reducing the RMS of LIM from 2.08 cm to 1.52 cm. Statistical analysis in Fig. 8 further highlighted NIM's robustness. Its median error approached zero with a narrower interquartile range spanning (IQR) -1.5 to 0.5 cm compared to LIM's -2 to 0.5 cm. The model also showed fewer outliers and tighter error within ± 5 cm in kernel density plots.

Low-latitude case (HK-1, May 24, 2024)

For low-latitude regions, the HK-1 dataset (March 24, 2024) revealed similar trends. Preliminary interpolation tests were conducted (T. Liu et al. 2024a, b). With HKST as the master station and HKSC as the user (9.3 km baseline), NIM consistently outperformed LIM, particularly during noon–18:00 local time (Fig. 9). During peak ionospheric activity (14:00–16:00), LIM errors exceeded 3 cm for multiple satellites, while NIM maintained below 3 cm. A focused analysis of PRNs 11, 14, 19, and 6 (16:00–16:24) showed NIM improving precision by 0.5–1 cm. During post-sunset, NIM retained better alignment with reference values. Quantitative metrics in Table 2 confirmed these observations: during active periods from 12:00 to 00:00, NIM reduced mean error by 35% cm, from 1.11 cm to 0.72 cm, and decreased RMS by 33% cm, from 1.47 cm to 0.99 cm. Quiet periods

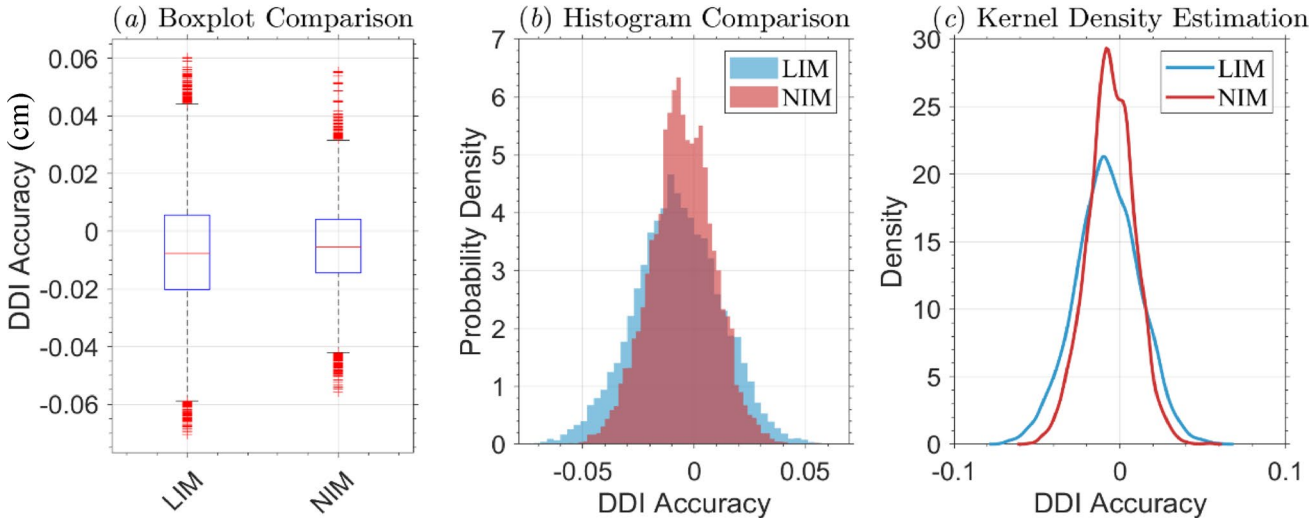

Fig. 8 Boxplot comparison and statistical results at Melbourne on May 1, 2024

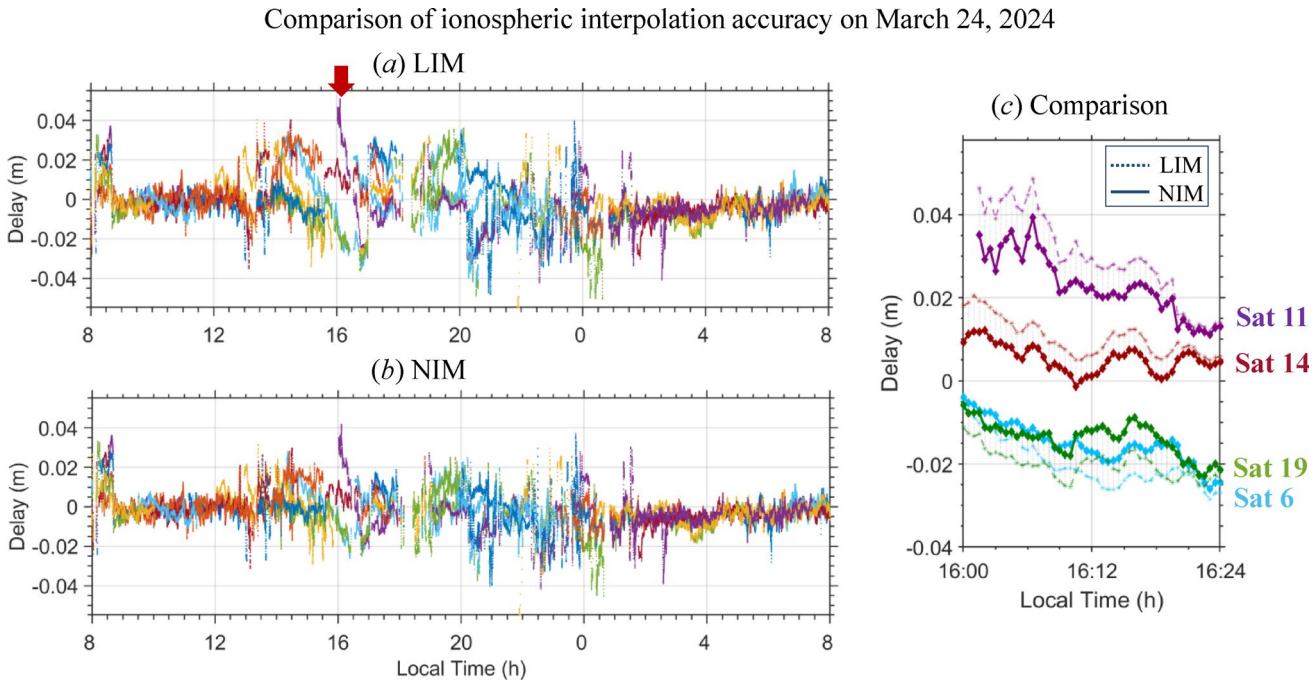

Fig. 9 Interpolation accuracy on March 24, 2024, via LIM (subfigure a) and NIM (subfigure b). The 16:00–16:24 in subfigure a (marked by red arrow, the time of large ionospheric gradient during sunset) is enlarged in subfigure c

Table 2 Statistics on the interpolation results of LIM and NIM on 24 March 2024

Ionosphere state	Method	Mean (cm)	RMS (cm)	3σ (cm)
Active (sunset and post-sunset)	LIM	1.11	1.47	2.90
	NIM	0.72	0.99	2.03
Quiet (wee hours and sunrise)	LIM	0.55	0.76	1.57
	NIM	0.49	0.67	1.40

showed smaller consistent gains, with 11% cm mean error reduction and 12% cm RMS improvement.

Statistical performance during the geomagnetic storm on May 2024

We further evaluated the model's robustness using the HK-2 dataset during the severe May 8–14, 2024 geomagnetic storm. With HKPC as the master station and HKMW forming a 4.8 km baseline user connection, Fig. 10 demonstrates NIM's stability under extreme conditions. On May

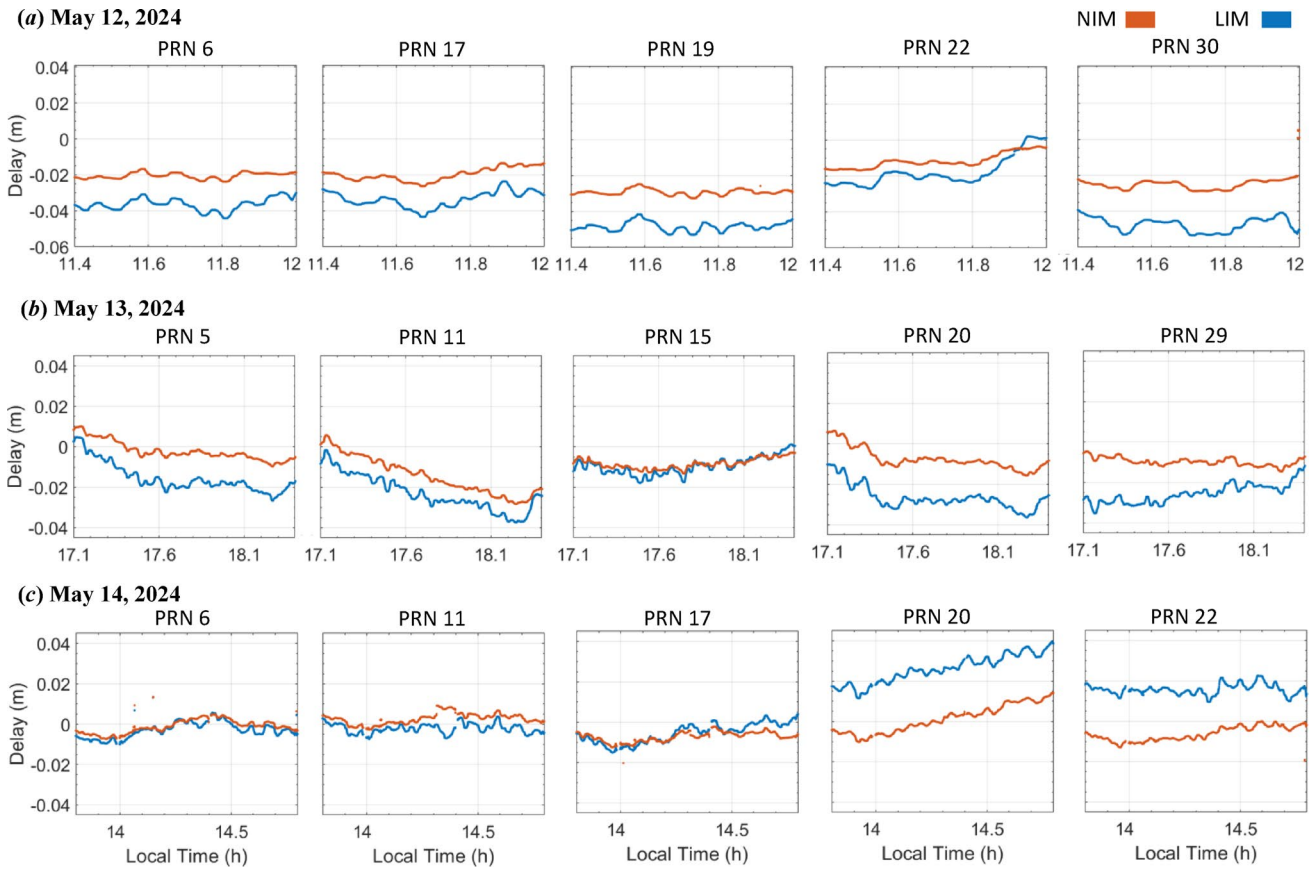

Fig. 10 A comparison of the results obtained using NIM and LIM against the reference values from double-difference ionospheric delays

Table 3 Statistics on the interpolation results of LIM and NIM on May 8–14, 2024

	MEAN (cm)		RMS (cm)		3σ (cm)	
DOY	LIM	NIM	LIM	NIM	LIM	NIM
129	3.1	1.5	5.6	2.6	14.0	6.5
130	2.6	1.5	5.2	3.3	13.4	8.8
131	1.7	1.0	2.2	1.3	4.2	2.4
132	3.7	1.9	5.7	3.0	13.0	7.1
133	1.8	0.9	3.2	1.7	7.9	4.2
134	1.7	1.0	2.4	1.2	5.0	2.4
135	2.2	1.1	3.6	1.7	8.7	3.9

12 (Fig. 10a), NIM reduced positioning errors by 50% for PRNs 6, 7, 13, 22, and 30, notably cutting PRN 6 errors from 4 cm under LIM to 2 cm. The following day (Fig. 10b), NIM maintained precision below 1.5 cm for PRNs 5, 11, and 20 while LIM showed 3–4 cm variations. During the storm's peak activity on May 14 between 14:00–14:30 UTC (Fig. 10c), NIM consistently delivered under 2 cm accuracy for PRNs 11, 17, and 20, where LIM errors exceeded 3 cm. As depicted in Fig. 10, the interpolation results for certain satellites, such as PRN 22 on May 12, display relatively pronounced time-varying characteristics. This phenomenon is likely attributable to that the movement of the IPP traversed areas with large ionospheric gradients.

Statistical analysis in Table 3 confirms NIM's consistent performance advantage throughout the storm period. Mean error decreased from 2.4 cm (LIM) to 1.1 cm (NIM), with RMS error halved from 4.0 cm to 2.1 cm. The 3σ error range narrowed by 47%, dropping from 9.5 cm to 5.0 cm. The most substantial improvement occurred on DOY 132 (May 11), coinciding with the storm's peak intensity, where NIM reduced the 3σ range from 13.0 cm to 7.1 cm compared to LIM.

In terms of physical mechanisms, we find that the geomagnetic storm on May 11, 2024 (DOY 132), marked by a Dst index drop to -413 nT, significantly increased TEC in the ionosphere. This increase was primarily driven by

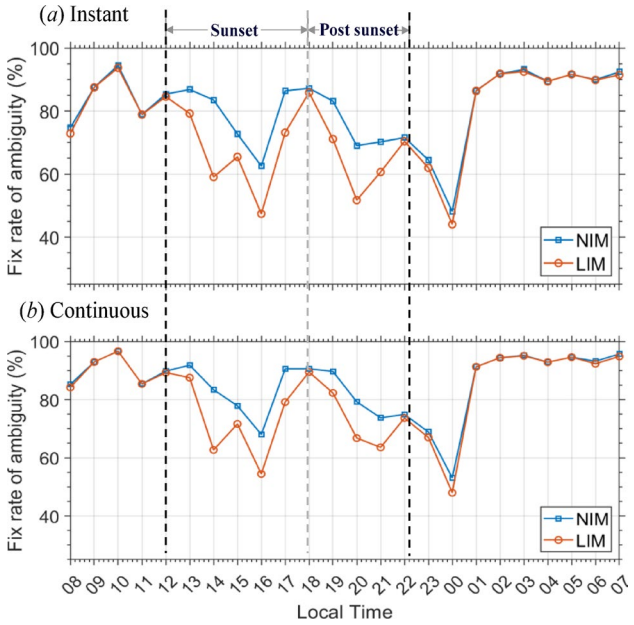

Fig. 11 Fix rate of ambiguity resolution for the baseline solution of the virtual observation station and HKSC on March 24, 2024

intense prompt penetration electric fields (PPEFs), which enhanced the eastward electric field at low latitudes, raising plasma to higher altitudes and intensifying the EIA crests (Tsurutani et al. 2008). Furthermore, coronal mass ejection (CME) activity from active region 13,664 on DOY 129 and 130 could contributed to increased ionospheric gradients and turbulence by intensifying interplanetary disturbances (Romano et al. 2024). These pre-storm conditions likely account for the larger positioning errors observed on these days, as previous studies noted elevated TEC during sunset prior to the May 11 storm at Bhopal (Jain et al. 2024), Mediterranean sector (Spogli et al. 2024) of the north crest of EIA. Together, the pre-storm and storm-phase behaviors of the ionosphere resulted in more pronounced spatial gradients in low-latitude regions. Under these conditions, the NIM demonstrated improved performance by effectively modeling the large-scale gradients between satellites, leading to more accurate DDI interpolation.

Positioning performance

Ambiguity resolution and positioning accuracy

The enhanced ionospheric interpolation accuracy significantly impacts ambiguity resolution success rates, as demonstrated in Fig. 11 for instant-epoch and continuous-epoch scenarios on March 24, 2024, with HK-1 dataset. During sunset (12:00–18:00) and post-sunset periods (18:00–22:00), when Hong Kong lies within the EIA crest region (Huang et al. 2023), and when the intensified eastward electric fields driving secondary spatial gradient peaks (Hao et al. 2024), NIM achieves notable improvements over LIM. The ambiguity resolution success rate saw a 9.4% rise for single-epoch cases and a 7.6% boost for continuous-epoch scenarios during periods of heightened ionospheric activity. Peak improvements occurred at 14:00, where success rates jumped from approximately 60% to over 80% as detailed in Table 4. Performance remained comparable between both models during early morning hours from 1:00 onward. NIM delivered operational benefits by cutting convergence time by 22% and enhancing post-convergence accuracy by 22% in the east-north and 5% in the vertical direction, highlighting its practical advantages.

Figure 12 quantifies these improvements through error distribution analyses. In instantaneous ambiguity resolution, NIM shrunk planar error ellipse dimensions from 5.7 cm × 7.4 cm under LIM to 4.3 cm × 5.2 cm. Continuous-epoch scenarios showed parallel gains, narrowing dimensions from 4.9 cm × 6.6 cm to 4.0 cm × 5.2 cm. Vertical error patterns in subplots *a*.3 and *b*.3 reveal tighter clustering of NIM errors near zero, with three-sigma boundaries shrinking 25–30% versus LIM. These outcomes validate NIM's enhanced ability to counteract ionospheric spatial decorrelation effects, providing clearer evidence of its technical superiority in handling gradient-driven positioning errors.

Statistical performance during the geomagnetic storm May 2024

Figure 13 compares the average interpolation accuracy and ambiguity resolution success rates of LIM and NIM for each hour during the May 2024 geomagnetic storm with HK-2 dataset. Subplots (*a*) and (*b*) depict interpolation errors and ambiguity resolution success rates, respectively, with local

Table 4 Statistics on the positioning results of LIM and NIM on 24 March 2024

Ionosphere state	Method	Ambiguity fix rate		Converged accuracy		Time to convergence (s)
		Instantaneous	Continuous	E-N (cm)	U (cm)	
Active	LIM	67.5%	74.0%	1.8	3.8	2.3
	NIM	76.9%	81.6%	1.4	3.6	1.8
Calm	LIM	84.2%	88.5%	1.1	3.8	1.6
	NIM	84.7%	89.0%	1.1	3.7	1.5

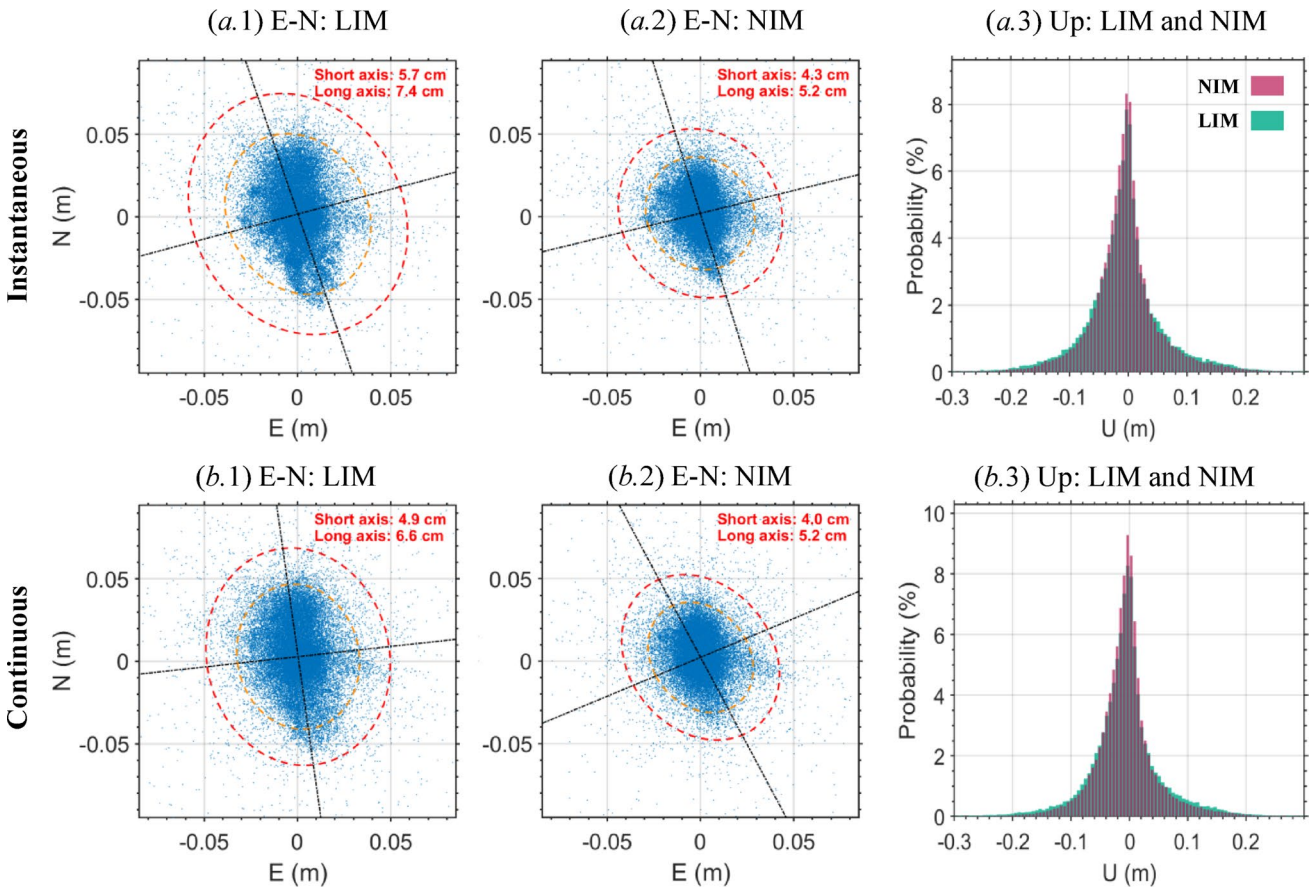

Fig. 12 Positioning statistics of E-N and U direction from instant and continuous ambiguity resolution on March 24, 2024

time (*x*-axis) and day of year (*y*-axis) represented across color-coded scales. NIM demonstrates consistently lower DDI interpolation errors compared to LIM, particularly during daytime and geomagnetically active periods such as DOY 132 (May 11, 2024). During post-sunset, NIM maintains errors below 4 cm, whereas LIM exhibits fluctuations exceeding this threshold. Similarly, NIM achieves ambiguity resolution success rates above 80% on DOY 129, 130, and 132, outperforming LIM, which frequently drops below 60%. These results highlight NIM's superior capability to model ionospheric variations in low-latitude regions under disturbed conditions, directly enhancing ambiguity resolution reliability.

Table 5 quantifies NIM's improvements over LIM in GNSS ambiguity resolution and positioning accuracy from May 8–14, 2024. NIM achieves a 5–10% higher ambiguity resolution success rate and reduces convergence time by approximately 33%, averaging 1.8 s compared to LIM's 2.7 s. Positioning accuracy shows marginal yet consistent gains: horizontal east-north errors decrease by 0.1 to 0.3 cm, while vertical up errors improve by 0.3 to 0.6 cm. Notably, on May 11 Day of Year 132 during peak geomagnetic activity, NIM maintains stable performance, demonstrating its resilience under extreme ionospheric dynamics.

Local ionospheric indices were calculated for collaborative analysis for the impact of ionospheric scintillation (Luo et al. 2020a; Liu et al. 2022). Two days of this week shows ionospheric scintillation, as shown in Fig. 14. During the period from 22:00 to 05:00 on DOY 130, both ROTI and S4 indices exhibited sustained ionospheric scintillation. This corresponded to the timeframe between 22:00 on DOY 130 and 05:00 the next day in Fig. 13, during which ambiguity resolution success rates predominantly remained below 60% regardless of interpolation method. Through fault detection and exclusion (FDE), satellites experiencing scintillation were excluded from DDI estimation process and subsequent interpolation steps, with only satellites maintaining normal carrier-phase observations being utilized. Similarly, mild scintillation events occurred during the early hours of DOY 132 (May 11–12). On most time on the other 5 days, DDI computations proceeded normally, allowing uninterrupted interpolation processes.

Figure 15 further illustrates NIM's advantages in positioning accuracy during continuous ambiguity resolution. Error ellipses for NIM (subplot *b*) are significantly smaller

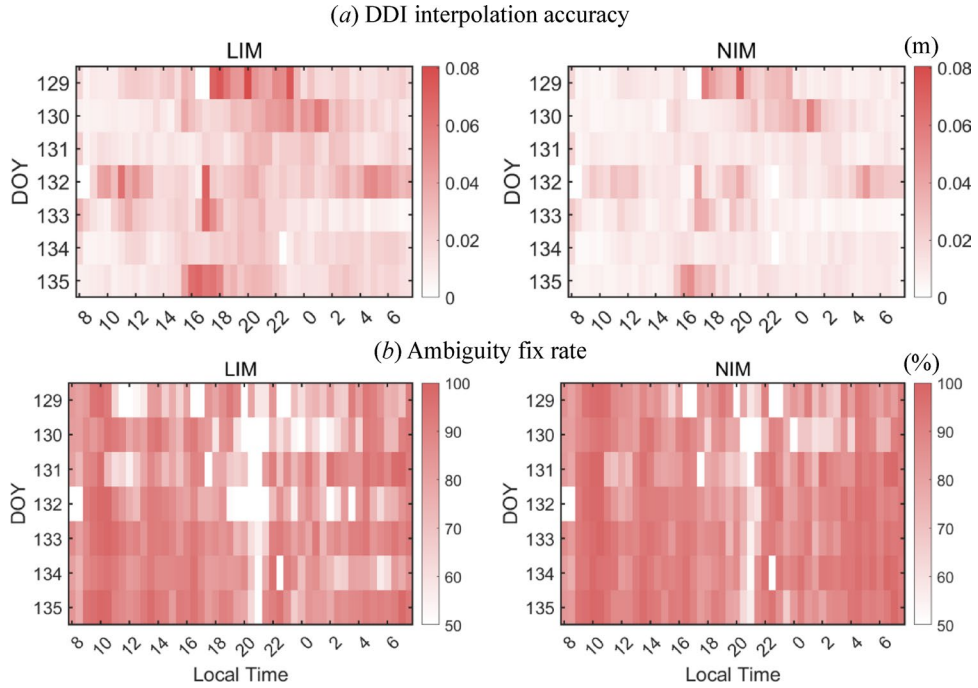

Fig. 13 The relationship between DDI estimation accuracy and ambiguity resolution success rate

Table 5 A comparison of the statistical results for interpolation accuracy on a daily basis from May 8th to 14th, 2024

	Fix rate		Time to convergence (s)		E-N (cm)		U (cm)	
DOY	LIM	NIM	LIM	NIM	LIM	NIM	LIM	NIM
129 (May 8)	72.1%	80.8%	2.6	1.7	1.3	1.1	4.4	4.1
130 (May 9)	72.0%	80.7%	2.7	1.8	1.3	1.1	4.4	4.0
131 (May 10)	74.7%	86.6%	3.1	2.0	1.4	1.1	4.7	4.4
132 (May 11)	67.1%	77.8%	2.5	1.9	1.4	1.2	3.6	3.8
133 (May 12)	78.1%	86.9%	2.4	1.6	1.2	1.1	4.3	3.8
134 (May 13)	75.0%	86.5%	3.4	2.1	1.3	1.1	5.1	4.5
135 (May 14)	72.8%	83.0%	2.7	1.9	1.4	1.2	4.7	4.2

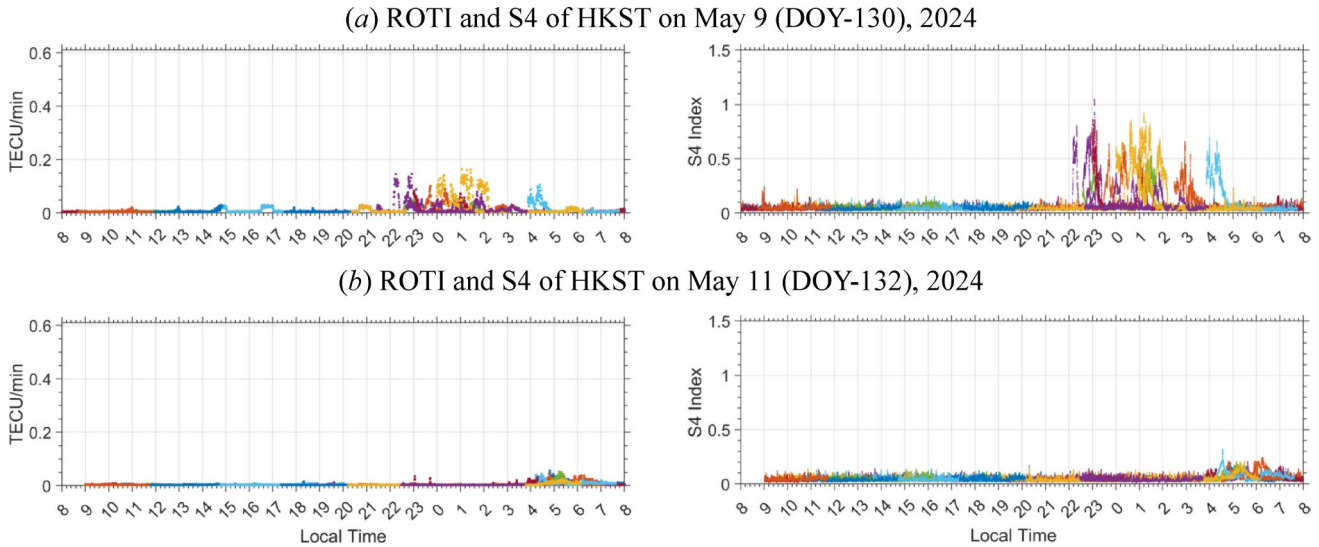

Fig. 14 ROTI and S4 of HKST on May 9 and 11, 2024

than those of LIM (subplot *a*), with short and long axes reduced from 6.2 cm and 7.2 cm to 3.7 cm and 4.4 cm, respectively. This contraction reflects a more precise error distribution. Subplot (*c*) reinforces these findings: NIM's elevation errors (light purple) cluster closer to zero, whereas LIM exhibits broader dispersion.

The observed improvements in positioning accuracy with NIM are largely due to its more precise estimation of ionospheric delays, which directly enhances the ambiguity resolution process. While accurate ionospheric delay estimates improve the float solution's precision, the primary benefit lies in the increased success rate of ambiguity resolution, enabling the float solution to transition into a fixed solution (Mi et al. 2019). In addition to the phase ambiguity resolution method used in RTKlib, NIM could also be contribute to other RTK algorithms such as Melbourne-Wübbena (MW) combination. Once wide-lane ambiguities are resolved, the accuracy of the ionospheric delay estimate becomes critical for addressing narrow-lane ambiguities (Colombo et al. 2002). Virtual observations generated at the user end by NIM provide an ionospheric delay estimation closely aligned with the user's true ionospheric conditions. This minimized DDI brings the narrow-lane and L1 float solutions closer to their integer values, thereby simplifying and enhancing the reliability of the ambiguity resolution process (Zhu et al. 2023; J. Wang & Yu 2024). Moreover, NIM's advanced ionospheric modeling may reduce the risk of incorrect ambiguity resolution, particularly under low ratio thresholds.

Discussion

Through the analysis of the results, we can compare the fundamental distinctions between the LIM and NIM as follows. Additionally, we will address the limitations of NIM and the remaining challenges for current network RTK encountered during the data processing.

Comparison of LIM and NIM in principles

Figure 16 illustrates the unique aspects of NIM compared to the traditional LIM approach:

Input Terms of the Function: LIM primarily relies on DDI as its input, while, NIM incorporates both the DDI and its gradient, allowing account for the spatial nonlinearity of ionospheric delays more effectively. This gradient term in NIM can be calculated flexibly, either through time differencing of dual-frequency carrier phases or other approaches that capture inter-satellite ionospheric variability.

Dependencies of Detrending Function: LIM relies solely on station coordinates or IPP differences between stations for detrending. In contrast, NIM utilizes IPP differences between both satellites and stations, incorporating inter-satellite distances to address and mitigate the inter-satellite gradient. This approach allows NIM to robustly tackle the nonlinear spatial ionospheric variations that are especially pronounced in low-latitude regions.

It is worth noting that in the composite function of the NIM framework, station coordinates are exclusively associated with linear delays, while IPP gradients are solely linked to nonlinear delays. Consequently, whether station coordinate detrending serves as the outer function and IPP processing as the inner function, or vice versa—this merely represents a difference in computational sequence and theoretically does not affect the final outcome.

Limitation and remaining challenges

Ionospheric gradients at low latitudes during solar maxima are a significant factor affecting network RTK positioning. While the NIM method demonstrates superior performance

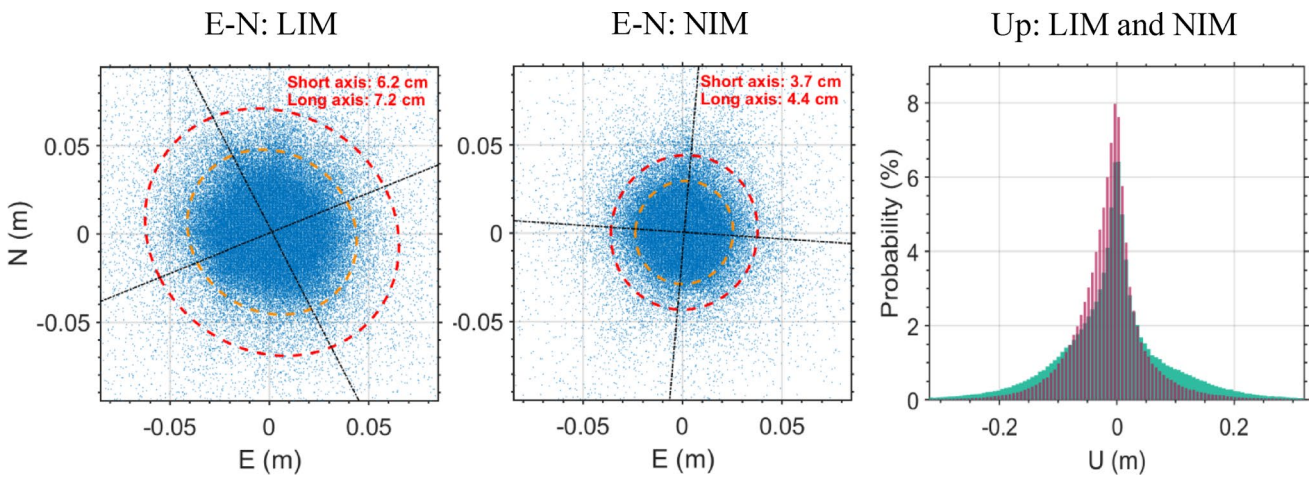

Fig. 15 Positioning statistics from continuous ambiguity resolution on May 8–14, 2024

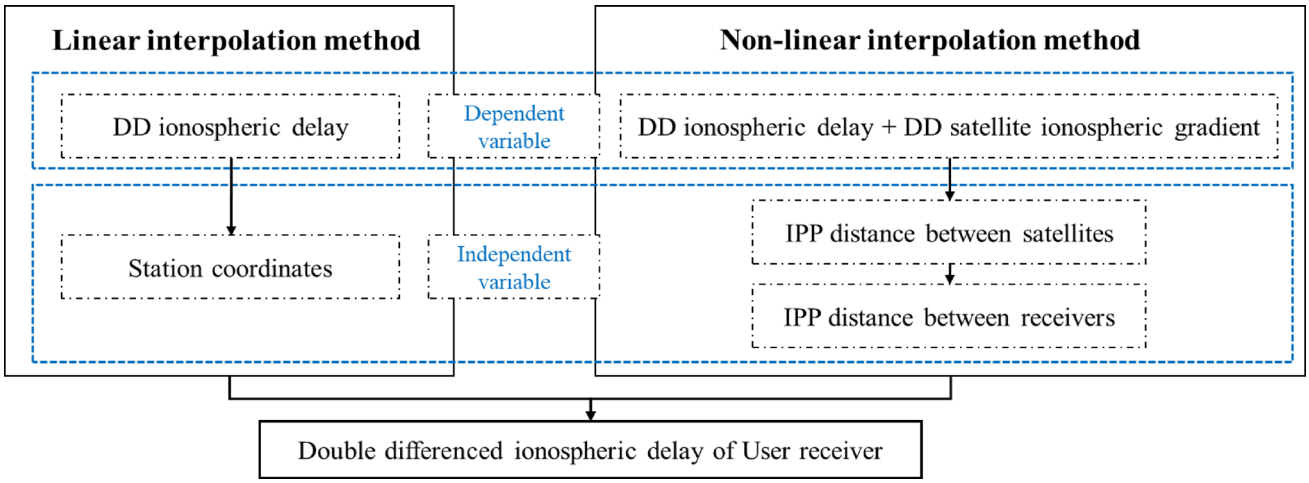

Fig. 16 The workflow of the nonlinear interpolation method and its comparison with the linear interpolation method

compared to traditional approaches, in the actual data-processing process, it has been found that low-latitude network RTK still faces unresolved issues related to the ionosphere. A summary of these issues is presented below.

A key limitation of the interpolation framework is its reliance on right resolution of double-difference ambiguities between master and reference stations. First, severe ionospheric scintillation can disrupt RTK services, and no fully reliable DDI exists. One mitigation strategy involves predicting and excluding time intervals or satellites likely impacted by plasma bubbles (Liu et al. 2022; Nie et al. 2024). However, regardless of the approach, scintillation degrades carrier-phase observation quality, rendering carrier-phase-based ionospheric delay calculations and subsequent interpolation unfeasible. Consequently, NIM is designed to address delays introduced by nonlinear ionospheric gradients, not scintillation-induced issues.

Even under non-scintillation conditions, robust preprocessing and quality control are critical. Effectively handling anomalies such as cycle slips could enhancing DDI estimation for more reliable RTK performance. Additionally, parameter settings, e.g., ambiguity resolution thresholds (Luo et al. 2020b), must be adjusted based on baseline length and ionospheric activity levels. The current ratio-based ambiguity resolution criterion, for instance, may prove suboptimal in highly active ionospheric regions: low ratio thresholds (e.g., <2) increase the risk of incorrect ambiguity fixes, while high thresholds reduce resolution success rates. Developing a more reliable method for determining ambiguity resolution (Gu et al. 2024), and its success rate (Ciuban et al. 2024; P. Teunissen 2024), and accuracy rate (W. Chen et al. 2022) is therefore essential.

Further, despite NIM's improvements, challenges remain in low-latitude regions where ionospheric effects dominate RTK errors. NIM still produces some vertical positioning outliers exceeding 20 cm, possibly due to its equal weighting of longitudinal and latitudinal ionospheric gradients (Hao et al. 2024; Y. Yang et al. 2024a, b). Adjusting the model to prioritize latitudinal variations may enhance accuracy. In addition to this, the current NIM method primarily focuses on the ionospheric gradients along the IPP trajectory. Inter-satellite modeling of ionospheric gradients orthogonal to the IPP trajectory could potentially contribute to further enhancing the interpolation accuracy.

Conclusion

This study presents the NIM as an advanced solution for mitigating ionospheric spatial gradients along IPP trajectory in network RTK systems, particularly under the challenging conditions of long baselines and low-latitude regions.

Comprehensive analysis spanning mid and low latitudes, show that it can improve the interpolation accuracy fall in ± 5 cm in most epochs, outperforming LIM's ± 6–7 cm range. The notable improvements brought about by NIM are primarily evident during periods of significant ionospheric gradients, specifically around sunset and post-sunset hours. This is likely linked to the ionospheric gradients induced by phenomena such as the EIA. During the May 2024 geomagnetic storm, NIM demonstrated superior performance, reducing DDI interpolation errors by 30% compared to LIM, with RMS values stabilizing below 2 cm even during peak storm activity (Dst $= -413$ nT). This enhancement directly translated to a 10% increase in ambiguity resolution success rates and a 33% reduction in convergence time, enabling horizontal and vertical positioning accuracies of 1.1–3.8 cm, respectively.

Key to NIM's success is its dual incorporation of station coordinates and IPPs, which effectively detrend spatial

variations along IPP trajectories. By leveraging GAIM, NIM minimizes residual gradients that traditional LIM fails to address, thereby aligning float solutions closer to integer values and enhancing ambiguity resolution reliability.

Despite these advancements, for DDI interpolation, NIM's equal weighting of longitudinal and latitudinal gradients may require recalibration, with prioritization of latitudinal variations likely to further improve accuracy. Additionally, for positioning, the reliance on ratio-based ambiguity resolution thresholds remains suboptimal during severe scintillation events, necessitating adaptive criteria to balance success rates and reliability.

Acknowledgements This work was supported by the University Grants Committee of Hong Kong under General Research Fund (GRF) (15212525 and 15229622), the National Natural Science Foundation of China (Grant No. 42404052), and the Guangdong-Hong Kong Technology Cooperation Funding Scheme (GHP/033/22SZ)

Author contributions T.L.: Methodology, Formal Analysis, Investigation, Data Curation, Validation, Visualization, Writing—Original Draft. W.C.: Conceptualization, Methodology, Formal Analysis, Investigation, Project Administration, Supervision, Funding Acquisition. X.M.: Validation, Formal Analysis, Writing—Review & Editing, Supervision, Project Administration, Funding Acquisition. X.C.: Software, Investigation, Writing—Review & Editing. Y.Y.: Software, Data Curation, Project Administration. J.D.: Software, Visualization. TX.L: Software, Data Curation. Y.W.: Formal Analysis. D.W.: Supervision, Funding Acquisition. All authors reviewed and approved the final manuscript.

Funding Open access funding provided by The Hong Kong Polytechnic University

Data availability The global ionosphere maps data of Center for Orbit Determination in Europe (CODE) are available from the Crustal Dynamics Data Information System (https://cddis.nasa.gov/) via registration, and also collected by the Chinese Academy of Sciences and can available via the FTP server: ftp://ftp.gipp.org.cn/product/ionex.The RINEX data of Hong Kong CORS stations are available for download at: https://rinex.geodetic.gov.hk/rinex3/; The Dst index data can be accessed at: https://wdc.kugi.kyoto-u.ac.jp/dstae/index.html.

Declarations

Conflict of interest The authors declare no competing interests.

References

Al-Shaery A, Lim S, Rizos C (2011) Investigation of different interpolation models used in Network-RTK for the virtual reference station technique. J Global Positioning Syst 10:136–148. https://doi.org/10.5081/jgps.10.2.136

Chen W, Hu C, Chen Y, Ding X (2001a) Rapid static and kinematic positioning based on GPS active network. Geomatics Inf Sci Wuhan Univ 26:518–523

Chen W, Hu C, Chen Y, Ding X, Simon K (2003) GPS rapid static and kinematic positioning based on GPS active network. Geo-Spat Inf Sci 6:5–11. https://doi.org/10.1007/BF02826694

Chen W, Xu Y, Weng D, Ji S (2022) A geometry-based ambiguity validation (GBAV) method for GNSS carrier phase observation. J Glob Position Syst 18:28–40. https://doi.org/10.5081/jgps.18.1.28

Chen J, Zhi N, Lv Z, Xu F, Lu M, Feng S (2024) Global and local consistency methodology for ionospheric dSTEC interpolation. IEEE Trans Geosci Remote Sens 62:1–16. https://doi.org/10.1109/TGRS.2024.3446842

Chen W, Hu C, Chen Y, Ding X (2001b) Rapid static and kinematic positioning with Hong Kong GPS active network. In: Proceedings of the 14th International Technical Meeting of the Satellite Division of The Institute of Navigation (ION GPS 2001), Salt Lake City, UT, pp. 346–352.

Cheng J, Zhao G, Zang N, Cheng S, Chen S, Yao J (2024) A novel piecewise linear transformation to moderate regional boundary effect on real-time regional ionospheric map (RT-RIM). Measurement 236:115050. https://doi.org/10.1016/j.measurement.2024.115050

Ciuban S, Teunissen PJ, Tiberius CC. (2024). GNSS Positioning Safety: Probability of Positioning Failure and its Components. In: Proceedings of the 37th International Technical Meeting of the Satellite Division of The Institute of Navigation (ION GNSS+ 2024), Ciuban, pp. 2228–2249.

Colombo OL, Hernandez-Pajares M, Juan JM, Sanz J (2002) Wide-area, carrier-phase ambiguity resolution using a tomographic model of the ionosphere. Navigation 49:61–69. https://doi.org/10.1002/j.2161-4296.2002.tb00255.x

Cui J, Tang W, Jin L, Deng C, Zou X, Gu S (2018) An improved ionosphere interpolation algorithm for network RTK in low-latitude regions. GPS Solutions 22:1–11. https://doi.org/10.1007/s10291-018-0778-y

Dai L, Han S, Wang J, Rizos C (2003) Comparison of interpolation algorithms in network-based GPS techniques. Navigation 50:277–293. https://doi.org/10.1002/j.2161-4296.2003.tb00335.x

Fotopoulos G (2000) Parameterization of carrier phase corrections based on a regional network of reference stations. In: Proceedings of the 13th international technical meeting of the satellite division of the institute of navigation (ION GPS 2000), Salt Lake City, UT, pp. 1093–1102.

Gu S, Fang L, Jiang W (2024) Multiple integer candidates ambiguity resolution: a unification ambiguity resolution algorithm. Satellite Navigation 5:21. https://doi.org/10.1186/s43020-024-00141-w

Hao H, Zhao B, Yue X, Ding F, Li G, Sun W, Ren Z, Liu L (2024) Latitudinal characteristics of the post-sunset enhancements in ionospheric electron density during the geomagnetic quiet period in May 2021 over East-Asian region. J Geophys Res Space Physics 129:e2024JA033047. https://doi.org/10.1029/2024JA033047

He L, Zhu Q, Wang C (2024) Comprehensive analysis of the equatorial ionization anomaly based on global ionospheric maps with a high spatiotemporal resolution. Adv Space Res 74:16. https://doi.org/10.1016/j.asr.2024.06.047

Hong J, Tu R, Zhang S, Li F, Liu M, Lu X (2022) Inter-satellite single-difference ionospheric delay interpolation model for PPP-RTK and its positioning performance verification. Remote Sens 14:4153. https://doi.org/10.3390/rs14174153

Huang F, Lei J, Luan X, Li G, Wang Y, Zhu Y, Chen J, Owolabi C, Dou X (2023) Dynamic processes associated with prominent ionospheric variations in a narrow longitudinal zone near the EIA crest region as revealed by ICON satellite and ground Beidou receiver observations over South Asia. J Geophys Res Space Physics 128:e2023JA031981. https://doi.org/10.1029/2023JA031981

Jain A, Trivedi R, Jain S, Choudhary R (2024) Effects of the super intense geomagnetic storm on 10–11 May, 2024 on total electron content at Bhopal. Adv Space Res. https://doi.org/10.1016/j.asr.2024.09.029

Li P, Cui B, Hu J, Liu X, Zhang X, Ge M, Schuh H (2022a) Ppp-rtk considering the ionosphere uncertainty with cross-validation. Satellite Navigation 3:10. https://doi.org/10.1186/s43020-022-00071-5

Li W, Li Z, Wang N, Liu A, Zhou K, Yuan H, Krankowski A (2022b) A satellite-based method for modeling ionospheric slant TEC from GNSS observations: algorithm and validation. GPS Solutions 26:1–13. https://doi.org/10.1007/s10291-021-01191-2

Li X, Han J, Li X, Huang J, Shen Z, Wu Z (2023) A grid-based ionospheric weighted method for PPP-RTK with diverse network scales and ionospheric activity levels. GPS Solutions 27:191. https://doi.org/10.1007/s10291-023-01522-5

Liu T, Jiang Y, Ma Y, Yu Z, Xu G (2022) Maximum eigenvalue detection for local ionospheric anomaly-theory, cases, statistics, and potential application. Measurement 203:111990. https://doi.org/10.1016/j.measurement.2022.111990

Liu A, Li Z, Wang N, Li A, Zhang Z, Zhang Y (2024a) A gaussian variogram-based model of total electron content in the regional ionosphere of China. Space Weather 22:e2024SW004047. https://doi.org/10.1029/2024SW004047

Liu T, Mi X, Yang Y, Weng D, Chen W. (2024). Model the Ionospheric Gradients Between Satellites in Network RTK. In: Proceedings of the 37th International Technical Meeting of the Satellite Division of The Institute of Navigation (ION GNSS+ 2024), Baltimore, Maryland, pp. 3092–3100.

Luo X, Gu S, Lou Y, Cai L, Liu Z (2020a) Amplitude scintillation index derived from C/N 0 measurements released by common geodetic GNSS receivers operating at 1 Hz. J Geod 94:27. https://doi.org/10.1007/s00190-020-01359-7

Luo X, Gu S, Lou Y, Chen B, Song W (2020b) Better thresholds and weights to improve GNSS PPP under ionospheric scintillation activity at low latitudes. GPS Solutions 24:17. https://doi.org/10.1007/s10291-019-0924-1

Lyu S, Xiang Y, Zhang Y, Yang H, Pei L, Yu W, Turong T-K (2023) A consistent and grid-based regional slant ionospheric model with an increasing number of satellite corrections for PPP-RTK. GPS Solutions 27:97. https://doi.org/10.1007/s10291-023-01439-z

Lyu H, Hernández-Pajares M, Li M, Monte-Moreno E, Prol FS, Zhang H, Deng C, Liu J (2024) Global 3d ionospheric shape function modeling with kriging. J Geod 98:104. https://doi.org/10.1007/s00190-024-01908-4

Martyn D. (1955). Theory of height and ionization density changes at the maximum of a Chapman-like region, taking account of ion production, decay, diffusion and tidal drift. In: Physics of the Ionosphere. The Physical Society, Cavendish Laboratory, Cambridge, pp. 254.

Mi X, Zhang B, Yuan Y (2019) Stochastic modeling of between-receiver single-differenced ionospheric delays and its application to medium baseline RTK positioning. Meas Sci Technol 30:095008. https://doi.org/10.1088/1361-6501/ab11b5

Mitra S (1946) Geomagnetic control of region F2 of the ionosphere. Nature 158:668–669

Nie W, Wang F, Qiao Z, Xu T, Wang Y, Ye M, Hu L, Liu T (2024) Ionospheric irregularities coinciding with the 2023 Typhoon Saola: a multi-instrument study. J Geophys Res Space Physics 129:e2024JA033043. https://doi.org/10.1029/2024JA033043

Nigussie M, Jakowski N, Hoque M (2022) Characterization and climatological modeling of equatorial ionization anomaly (EIA) crest position. J Geophys Res Space Physics 127:e2022JA030798. https://doi.org/10.1029/2022JA030798

Ren H, Jiang Y, Liu T (2024) An anisotropic kriging for ionospheric delay interpolation with a wide area reference network. IEEE Trans Geosci Remote Sens 62:1–13. https://doi.org/10.1109/TGRS.2024.3508800

Romano P, Elmhamdi A, Marassi A, Contarino L (2024) Analyzing the sequence of phases leading to the formation of the active region 13664, with potential Carrington-like characteristics. Astrophys J Lett 973:L31. https://doi.org/10.3847/2041-8213/ad77cb

Saraçoğlu A (2024) Causal insights into GPS precision variability: an investigation into the ionospheric impact on GPS measurements throughout the solar cycle. Bull Geophys Oceanogr (BGO). https://doi.org/10.4430/bgo00438

Shi Z, Zhi N, Fu H, Wang D, Sui Y, Zhao Y, Feng S, Jin Y-Q (2022) A method for dSTEC interpolation: ionosphere kernel estimation algorithm. IEEE Trans Geosci Remote Sens 60:1–18. https://doi.org/10.1109/TGRS.2022.3218365

Slamet S, Zainal AH, Darmawan WD, Prayitno A, Susumu S, Unggul PD (2022) Construction of nominal ionospheric gradient using satellite pair based on GNSS CORS observation in Indonesia. Earth Planets Sp (Online). https://doi.org/10.1186/s40623-022-01633-2

Spogli L, Alberti T, Bagiacchi P, Cafarella L, Cesaroni C, Cianchini G, Coco I, Di Mauro D, Ghidoni R, Giannattasio F, Ippolito A, Marcocci C, Pezzopane M, Pica E, Pignalberi A, Perrone L, Romano V, Sabbagh D, Scotto C, Spadoni S, Tozzi R, Viola M (2024) The effects of the May 2024 Mother's Day superstorm over the Mediterranean sector: from data to public communication. Ann Geophys. https://doi.org/10.4401/ag-9117

St-Pierre C (1999) Improvement of OTF-kinematic GPS positioning over long distances using ionospheric regional modelling. Geomatica 53:395–403. https://doi.org/10.5623/geomat-1999-0056

Sun M, Liu T, Ding Z, Liu J, Huang Y, Zhang K, Fang S, Li S, Kong Q, Chen B (2025a) Real-time regional ionosphere modeling with RFR-net over China. Space Weather 23:e2024SW004237. https://doi.org/10.1029/2024SW004237

Sun M, Liu T, Liu J, Zhang K, Huang J, Chen B (2025b) Real-time precise point positioning performance in Hong Kong during May 2024 space weather events. J Space Weather Space Clim 15:36. https://doi.org/10.1051/swsc/2025033

Takasu T, Yasuda A (2009) Development of the low-cost RTK-GPS receiver with an open source program package RTKLIB. In: International symposium on GPS/GNSS. International Convention Center Jeju Korea Seogwipo-si, Republic of Korea, Korea, pp. 1–6.

Tang W, Jin L, Cui J, Shi C, Zhang Y (2016) GNSS network RTK regional ionospheric modelling studies and performance analysis. J Navig 69:211–224. https://doi.org/10.1017/S0373463315000636

Teunissen P (2024) On the optimality of DIA-estimators: theory and applications. J Geod 98:43. https://doi.org/10.1007/s00190-024-01859-w

Teunissen PJ. (1993). Least-squares estimation of the integer GPS ambiguities. In: Invited lecture, section IV theory and methodology, IAG general meeting, Beijing, China, pp. 1–16.

Tsurutani BT, Verkhoglyadova O, Mannucci A, Saito A, Araki T, Yumoto K, Tsuda T, Abdu MA, Sobral JHA, Gonzalez WD

(2008) Prompt penetration electric fields (PPEFs) and their ionospheric effects during the great magnetic storm of 30–31 october 2003. J Geophys Res Space Physics. https://doi.org/10.1029/2007JA012879

Vollath U, Buecherl A, Landau H, Pagels C, Wagner B. (2000). Multi-base RTK positioning using virtual reference stations. In: Proceedings of the 13th International Technical Meeting of the Satellite Division of The Institute of Navigation (ION GPS 2000), Salt Lake City, UT, pp. 123–131.

Wang J, Yu X (2024) Improving the fixed solution by processing the unmodeled errors in GNSS RTK long baseline positioning. GPS Solutions 28:164. https://doi.org/10.1007/s10291-024-01707-6

Wang P, Nie G, Liu H, Wen J, Wang Y, Shen H (2023) An ionosphere-weighted calibration method with multi-station network corrections. Adv Space Res 72:3982–3997. https://doi.org/10.1016/j.asr.2023.06.057

Wanninger L (1995a) Enhancing differential GPS using regional ionospheric error models. Bull Géodésique 69:283–291. https://doi.org/10.1007/BF00806740

Wanninger L. (1995b). Improved ambiguity resolution by regional differential modelling of the ionosphere. In: Proceedings of the 8th international technical meeting of the satellite division of the institute of navigation (ION GPS 1995), Palm Springs, CA, pp. 55–62.

Weng D, Ji S, Chen W, Li Z, Xu Y, Ye L (2015) Assessing and mitigating the effects of the ionospheric variability on DGPS. GPS Solutions 19:107–116. https://doi.org/10.1007/s10291-014-0372-x

Wübbena G, Bagge A, Seeber G, Böder V, Hankemeier P. (1996). Reducing distance dependent errors for real-time precise DGPS applications by establishing reference station networks. In: Proceedings of the 9th International Technical Meeting of the Satellite Division of The Institute of Navigation (ION GPS 1996). Institute of Navigation, Kansas City, MO, pp. 1845–1852.

Yang L, Fu Y, Zhu J, Shen Y, Rizos C (2024a) GNSS ionospheric integrity monitoring based on RBF-NN: constructing single-epoch snapshot GIVD and GIVE maps. J Geod 98:31. https://doi.org/10.1007/s00190-024-01838-1

Yang Y, Liu L, Zhao X, Han T, Tariq MA, Chen Y, Zhang H, Le H, Zhang R, Li W (2024b) A quantitative analysis of latitudinal variation of ionospheric total electron content and comparison with IRI-2020 over China. Adv Space Res 73:3808–3817. https://doi.org/10.1016/j.asr.2023.05.040

Zhang X, Ren X, Chen J, Zuo X, Mei D, Liu W (2022) Investigating GNSS ppp–rtk with external ionospheric constraints. Satellite Navigation 3:6. https://doi.org/10.1186/s43020-022-00067-1

Zhang J, Ren X, Mei D, Abdelaziz A, Zhang X, Pan G, Jiang K (2024a) Long-term analysis of NRTK positioning performances over one solar activity cycle from 2013 to 2023. GPS Solutions 28:179. https://doi.org/10.1007/s10291-024-01727-2

Zhang W, Wang J, Khodabandeh A (2024b) Regional ionospheric correction generation for GNSS PPP-RTK: theoretical analyses and a new interpolation method. GPS Solutions 28:139. https://doi.org/10.1007/s10291-024-01682-y

Zhou L, Huang D, Feng W, Chen W, Zhang X, Yan L (2019) Global precision analysis of carrier phase relative positioning in BeiDou navigation satellite system and United States global positioning system. Sci China Earth Sci 62:733–749. https://doi.org/10.1007/s11430-017-9287-3

Zhu F, Chen X, Ma L, Liu W, Zhang X (2023) S2l-rtk: temporal ionospheric modeling for RTK baselines varying from short to long. GPS Solutions 27:156. https://doi.org/10.1007/s10291-023-01505-6

Zhu F. (2019). GNSS/SINS/Vision Multi-sensors Integration For Precise Positioning and Orientation Determination. Unpublished Doctoral dissertation, Wuhan University.